High-Performance Doped Silver Films: Overcoming Fundamental Material Limits for Nanophotonic Applications

*Cheng Zhang, Nathaniel Kinsey, Long Chen, Chengang Ji, Mingjie Xu, Marcello Ferrera, Xiaoqing Pan, Vladimir M. Shalaev, Alexandra Boltasseva, and L. Jay Guo**

The field of nanophotonics has ushered in a new paradigm of light manipulation by enabling deep subdiffraction confinement assisted by metallic nanostructures. However, a key limitation which has stunted a full development of high-performance nanophotonic devices is the typical large losses associated with the constituent metals. Although silver has long been known as the highest quality plasmonic material for visible and near infrared applications, its usage has been limited due to practical issues of continuous thin film formation, stability, adhesion, and surface roughness. Recently, a solution is proposed to the above issues by doping a proper amount of aluminum during silver deposition. In this work, the potential of doped silver for nanophotonic applications is presented by demonstrating several high-performance key nanophotonic devices. First, long-range surface plasmon polariton waveguides show propagation distances of a few centimeters. Second, hyperbolic metamaterials consisting of ultrathin Al-doped Ag films are attained having a homogeneous and low-loss response, and supporting a broad range of high-*k* modes. Finally, transparent conductors based on Al-doped Ag possess both a high and flat transmittance over the visible and near-IR range.

The field of nanophotonics has ushered in a new paradigm of light manipulation by enabling deep subdiffraction confinement assisted by metallic nanostructures.[1–3] Negative index materials,[4] deep subdiffraction imaging,[5] flat optics,[6] angle-insensitive structural colors,[7] and optical invisibility[8] are just some of the important advances made by conjoining metal and dielectric optics. However, such nanophotonic/plasmonic systems have been limited due to their large optical losses. Consequently, there is now a significant effort to explore alternative materials (e.g., doped semiconductor,[9] transition metal nitride,[10] transparent conducting oxide,[11] 2D material,[12] etc.), and methods to improve the performance of plasmonic devices.[13,14] For many applications, optically thin films rather than bulk materials are utilized. However, the qualities of thin films can be significantly affected by their preparation procedure,[13] and usually deviate from those of bulk materials, due to reasons such as surface morphology, quantum confinement effect, built-in stress, etc.[15–17] Such a limitation is manifested in the case of silver (Ag), which is one of the most widely used plasmonic material. Ag has the highest figure of merit (FoM) for plasmonic applications (FoM = $\mathrm{Re}\{\varepsilon\}/\mathrm{Im}\{\varepsilon\}$[18]) of any plasmonic material in the visible and near infrared (NIR), and is widely available. However, it is well documented to have several fundamental problems, including difficulty to form continuous ultrathin films (<12 nm),[19] rough surface morphology (e.g., root-mean-square (RMS) roughness of 6 nm for a 15 nm film[20]), poor chemical and thermal stability, and inferior adhesion to substrates like silicon and fused silica. More specifically, with regards to the adhesion to standard substrates, Ag films

Dr. C. Zhang,[+] Dr. L. Chen, C. Ji, Prof. L. J. Guo
Department of Electrical Engineering and Computer Science
University of Michigan
Ann Arbor, MI 48109, USA
E-mail: guo@umich.edu

Dr. N. Kinsey, Prof. M. Ferrera, Prof. V. M. Shalaev, Prof. A. Boltasseva
School of Electrical and Computer Engineering
Birck Nanotechnology Center
Purdue University
West Lafayette, IN 47907, USA

M. Xu
Department of Materials Science and Engineering
University of Michigan
Ann Arbor, MI 48109, USA

M. Xu, Prof. X. Pan
Department of Chemical Engineering and Materials Science
University of California–Irvine
Irvine, CA 92697, USA

Prof. M. Ferrera
Institute of Photonics and Quantum Sciences
Heriot-Watt University, SUPA
Edinburgh, Scotland EH14 4AS, UK

Prof. X. Pan
Department of Physics and Astronomy
University of California–Irvine
Irvine, CA 92697, USA

[+]Present address: Center for Nanoscale Science and Technology, National Insitute of Standards and Technology, Gaithersburg, MD, 20899, USA

DOI: 10.1002/adma.201605177

can be removed by ultrasonic vibrations or even Scotch tape.[21] In addition, spontaneous dewetting of a thin Ag film occurs even at room temperatures[22] and can be greatly accelerated at modest temperatures ≈100 °C.[23]

We recently proposed a new approach to achieve ultrathin and smooth Ag films by introducing a small amount of Al dopants during the Ag film deposition. The Al atoms suppress the Vomer–Webber 3D growth mode of Ag, thereby promoting high-quality film formation at an early growth stage.[24] We demonstrated unprecedented wetting-layer-free thin Ag films achieved for a thickness down to 6 nm with a sub-nanometer roughness on various substrates, and employed them as semi-transparent electrodes in high-efficiency organic solar cells.[25] In this work, we further investigate Al-doped Ag's structural, thermal, and optical properties using various characterization techniques, and demonstrate several key nanophotonic components by capitalizing on its desirable properties. The devices include long-range plasmonic waveguides with a record low propagation loss, hyperbolic metamaterials with a low-loss and homogeneous response, and transparent conducting electrodes with a high transparency and negligible haze. Our work demonstrates the great potential of doped Ag films for high-performance nanophotonic devices.

For a thin metallic film embedded in a dielectric, the surface plasmon polaritons (SPPs) on both the upper and lower surfaces of the metal film couple with each other and form a symmetric long-range SPP (LR-SPP) mode.[26] Such modes have several advantages (e.g., wide operational bandwidth, ability to couple with other plasmonic structures, supporting both electrical and optical signals, etc.), and have been utilized in various plasmonic devices.[27–29] To construct efficient and robust LR-SPP waveguides, high-quality, and stable thin metallic films are required. Although Ag is a low-loss plasmonic material in the visible and NIR, it is rarely employed in LR-SPP waveguides due to its limitation in forming thin films, surface roughness, poor adhesion with substrates, and rapid degradation in ambient environments. In this work, we will show that Al-doped Ag overcomes many limitations of pure Ag (e.g., instability, rough surface morphology, poor adhesion to the substrates, etc.), and functions as a high-performance building block for LR-SPP waveguides.

We will first make a brief comparison of pure Ag film versus Al-doped Ag film. The upper part of **Figure 1**c shows the image of a 15 nm pure Ag film and a 7 nm Al-doped Ag film on fused silica substrates right after their deposition, where both exhibit uniform and similar appearances. However, pure Ag thin films are not stable in air, even at room temperatures, where this 15 nm film degrades rapidly after being taken out of the deposition chamber for only 30 min (lower part, Figure 1c). The corresponding scanning electron microscope (SEM) images of Ag films directly after deposition and after 30 min are shown in Figure SI-1 (Section S1.1, Supporting Information). A similar but slower degradation phenomenon has been reported for a 50 nm Ag film as well.[30] Consequently, although Ag has the highest FoM for plasmonic applications in the visible and NIR, its instability in air causes challenges in realizing LR-SPP waveguides. In contrast, the 7 nm thick Al-doped Ag film is stable under ambient conditions for over six months without any protective layer (Section S2.1, Supporting Information). The mechanism of such an enhanced stability will be discussed later in this section.

Figure 1a shows a SEM of a 7 nm Al-doped Ag film on a fused silica substrate, which exhibits a very smooth surface morphology (a 0.773 nm RMS roughness measured by atomic force microscopy). In contrast, pure Ag thin films below 10 nm are known to be discontinuous and consequently have very rough surface morphologies. For example, a 7 nm (nominal thickness) pure Ag is nonconductive/discontinuous, and has a rough surface (RMS roughness of 4.9 nm, Section S1.3, Supporting Information). One commonly used method to promote thin Ag growth is depositing a thin adhesion layer (e.g., germanium,[20] nickel,[31] or molybdenum oxide[32]). However, these adhesion layers generally induce additional losses (as they are poor plasmonic materials), which are especially detrimental for plasmonic structures since the optical field is enhanced at the metal–dielectric interface. Consequently, even a 1 or 2 nm thick wetting layer will cause a significant damping of the plasmonic mode.[33,34] Therefore, the method of adding adhesion layers are not suitable for fabricating LR-SPP waveguides. Additionally, it was recently shown that by treating the substrate with a thin layer of (3-mercaptopropyl) trimethoxysilane,[35,36] ultrathin gold (Au) can be deposited without inducing a significant plasmonic damping, and the film's adhesion with the substrate is enhanced. However, this method's applicability to silver as well as gold/silver based multilayer structures (e.g., hyperbolic metamaterials, negative index materials, etc.) needs to be further evaluated.

We find that the thermal stability of Al-doped Ag is significantly improved compared to pure Ag. Figure 1b shows the SEM of a 7 nm Al-doped Ag film after a thermal treatment at 500 °C in a nitrogen (N_2) environment for 3 min. While a pure Ag film dewets from the substrate and forms islands even at 300 °C (Section S1.2, Supporting Information), the Al-doped Ag film maintains its smooth surface morphology (RMS roughness changes from 0.773 to 0.836 nm after heating, Section S2.2, Supporting Information). In fact, after the thermal treatment, the optical loss of Al-doped Ag is further reduced. Figure 1d shows the measured permittivity of both as-deposited Al-doped Ag, and Al-doped Ag that undergoes an annealing treatment at 500 °C in a nitrogen (N_2) environment for 3 min (ellipsometry measurement procedures in the Experimental Section). Compared to the permittivity of as-deposited Al-doped Ag, the real part of permittivity of the annealed Al-doped Ag is similar, while the imaginary part of permittivity (which is proportional to the optical loss) is significantly reduced over a large wavelength range. An annealing treatment removes defects inside the film, and therefore, reduces the damping rate of electron scattering (lower optical loss).[37] Furthermore, such an improvement in the Al-doped Ag films can be observed for annealing cycles even as short as 10 s, making these films suitable for rapid thermal annealing treatments commonly used in semiconductor manufacturing.

One important question to ask is how the Al doping impacts the optical and electronic properties of the Ag film. Ag has one free electron per atom, while Al has three. Adding Al into Ag increases the density of free electrons, and therefore, modifies the plasma frequency (ω_p) of the resultant film. ω_p is

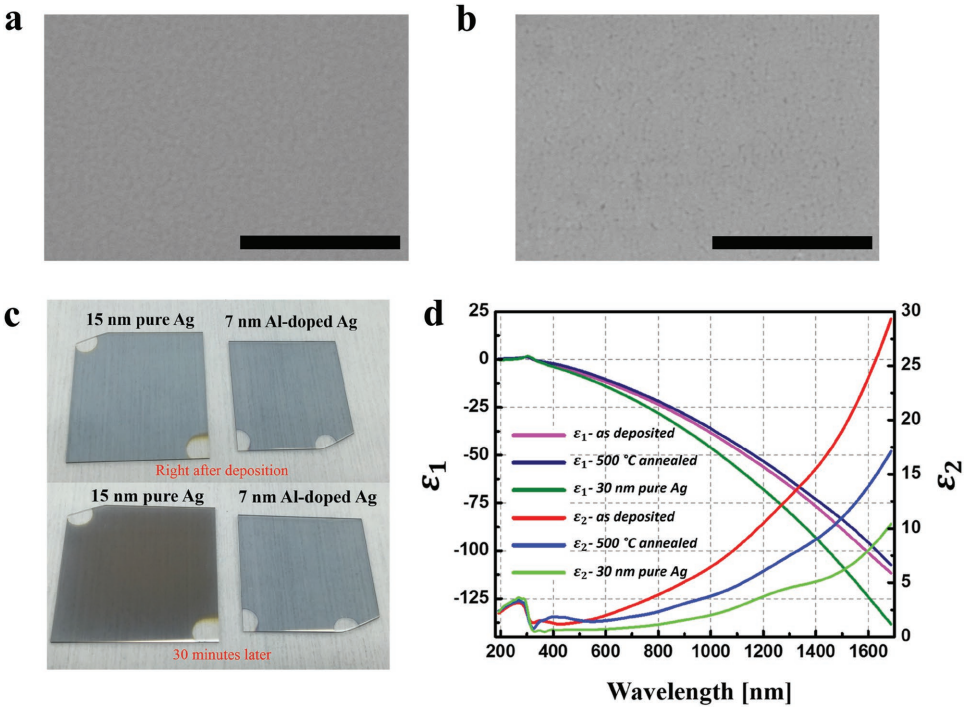

Figure 1. a) Scanning electron microscope (SEM) image of a 7 nm as-deposited Al-doped Ag film on fused silica substrate. The scale bar is 300 nm. b) SEM image of a 7 nm Al-doped Ag film on fused silica substrate, which underwent a 500 °C annealing treatment in N_2 for 10 s. The scale bar is 300 nm. c) Upper row: images of a 15 nm pure Ag and a 7 nm Al-doped Ag on fused silica substrates right after deposition, and Lower row: after 30 min in ambient air. d) Measured real and imaginary parts of permittivity of an as-deposited 7 nm Al-doped Ag film, a 7 nm film underwent annealing treatment (500 °C for 10 s in N_2), and a 30 nm as-deposited pure Ag.

proportional to the free electron density in the metal,[38] and there is a minimum in reflection intensity from a metal film near its ω_p. We experimentally characterized ω_p for Al-doped Ag and pure Ag films by measuring the reflection spectra of optically opaque (≈150 nm) films with a spectroscopic ellipsometer (M-2000, J. A. Woollam Inc.) at an angle of incidence of 45°. The measured reflection spectra are plotted in Figure SI-6 in Section S3 (Supporting Information). There is an 18 nm blue-shift of ω_p for Al-doped Ag compared to pure Ag (from 318 to 300 nm), due to the doping of Al atoms. Our measurement also corresponds with a previous study, where the plasma frequency of a 500 nm thick Al–Ag alloy film is characterized by the dip in reflection spectra at normal incidence, and there is a blue-shift in ω_p with the increase in Al concentration.[37] Since the Al concentration is low in our study, its effect on the electronic band structure is not obvious. For Ag, the interband transition from the occupied bound d states to unoccupied hybridized sp states causes an increased absorption in the UV range, which is denoted by a peak in the imaginary part of permittivity (ε_2).[39] As shown in Figure 1d, the peak wavelengths of interband transitions of Al-doped Ag and pure Ag overlap with each other. In addition, it can be seen that the loss of an ultrathin Al-doped Ag film is higher than a thicker (30 nm) pure Ag film, due to various reasons including the introduction of "Al impurities," and other factors related to a thin film (quantum confinement effect, built-in stress, etc.[15–17]). However, Al-doped Ag offers additional benefits when compared to pure Ag, such as ultrathin film formation, enhanced thermal and long-term stability, better adhesion with substrates, and improved 3D nanostructure coverage.

We should mention that there are some recent reports on binary mixture of noble metals (e.g., Ag–Au, Au–Cu, and Cu–Ag) to fabricate alloy films[40] or nanoparticles.[41] By adjusting the mixing ratio of the two metals, the band structures of the alloy can be modified, and the films exhibit new dielectric functions which cannot be modeled as the linear combination of pure metals. In contrast, our study focuses on achieving ultrathin (<10 nm) high-quality Ag films with a tiny amount of Al doping. Because the Al concentration is kept low, Al-doped Ag essentially maintains the dispersion properties of pure Ag.

To understand the film stability and ultrasmooth nature, we characterized Al-doped Ag by scanning transmission electron microscopy (STEM). **Figure 2**a shows an annular bright field (ABF) cross-sectional STEM image of a 7 nm Al-doped Ag film, which shows the film's polycrystalline structure. The measured film thickness by spectroscopic ellipsometer is 7.15 nm (Figure SI-7, Section S4, Supporting Information), and this corresponds well to the thickness value characterized by STEM. The distribution of Al and Ag atoms inside the film is characterized by X-ray energy-dispersive spectroscopy (EDS). To increase the signal to noise ratio and better facilitate the measurement, we used an ≈16 nm thick film in this study. The distribution of Al, Ag, and O atoms is mapped by the Ag_l, Al_k, and O_k peak intensity, respectively. The element mapping across the film for Ag, Al, and O atoms are shown in Figure 2b–d, respectively. It can be seen that Al and Ag atoms are mixed throughout the

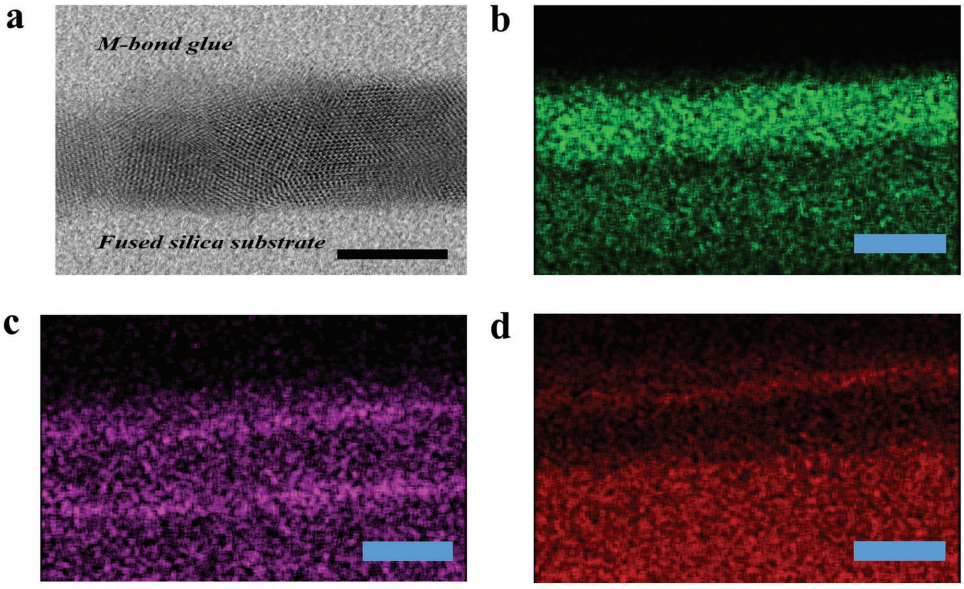

Figure 2. a) Annular bright field (ABF) cross-sectional scanning transmission electron microscope (STEM) image of a 7 nm Al-doped Ag film, which shows its polycrystalline structure. The scale bar is 5 nm. b–d) Cross-sectional element mapping of Ag (b), Al (c), and O (d) atom distributions in the film. The scale bar is 20 nm.

entire film. This observation corresponds to the fact that the mixture of Al and Ag forms a solid solution at both ambient and elevated temperature in the case of a low Al concentration, according to their phase diagram.[42] There is enrichment of Al near the top and bottom surfaces of the Al-doped Ag film, which is consistent to our previous X-ray photoelectron spectroscopy studies.[24] When the Al-doped Ag sample is taken out of the deposition chamber to the ambient environment, the oxygen (O) in-diffusion and Al out-diffusion lead to the formation of an oxidized Al network, which curbs the diffusion of Ag atoms and stabilizes the film. In contrast, a thin pure Ag film does not have such a "protection layer," and therefore, can easily dewet from the substrate. Finally, it is worth noting that although the concentration of Al at the boundaries of Al-doped Ag is higher than that of Al within the film, Ag atoms are still the majority of the film due to the low doping level of Al (deposition rates of Ag and Al are 1.109 and 0.072 nm s^{-1}, respectively). Therefore, the optical properties of Al-doped Ag resemble those of pure Ag.

Finally, the adhesion of Al-doped Ag films to many widely used substrates is also improved. Since pure Ag is easily removed by simple ultrasonication or even Scotch tape, precursor layers are typically required in order to improve adhesion. Indeed, the weak adhesion of Ag with the substrate (e.g., Si) has been utilized in the template-striping process to fabricate Ag nanostructures.[21] In contrast, Al-doped Ag has a sufficient adhesion with substrates to enable film processing in ultrasonic baths with many commonly used chemicals and solvents (e.g., resists, acetone, and isopropyl alcohol, etc.). This is a crucial property that profoundly simplifies the fabrication of many nanophotonic devices that require either planar or patterned thin films, including the LR-SPP waveguide which we are going to discuss in the next paragraph.

We have shown that Al-doped Ag outperforms pure Ag in terms of stability, ultrathin film formation, surface morphology, and adhesion to the substrate. In addition, its optical loss can be further reduced by a simple annealing treatment. All these merits facilitate the fabrication of high-performance LR-SPP waveguides. The Al-doped Ag based LR-SPP waveguides were fabricated on fused silica substrates and their performance was characterized (details are given in the Experimental Section). The device layout is shown in **Figure 3**a, where the index matching condition at 1.55 μm was achieved using an index-matching oil. The fabricated LR-SPP waveguide has a width of 9 μm and thickness of 10 nm (Figure 3b). The device performance is characterized by fiber end-coupling method (Figure 3c, details are given in Experimental Section). The out-coupled waveguide mode and its intensity profile along the vertical direction are shown in Figure 3d,e, respectively, where the vertical mode size ($1/e^2$ width) is found to be ≈9 μm along with a propagation loss (1/e decay length) of 0.66 dB cm^{-1}. This can be compared to simulations, shown in Figure 3f, where the simulated mode size and propagation loss for the 10 nm thick and 9 μm wide waveguide are 13 μm and 0.46 dB cm^{-1}, respectively. The discrepancy between simulation and measurement can be attributed to factors such as film thickness variation during deposition and lensing effects due to the index matching oil.[43] The experimentally demonstrated propagation length over 3 cm of Al-doped Ag waveguide is an order of improvement compared to those from similarly structured 10 nm thick, LR-SPP waveguides made of Au and TiN (Figure 3f),[43–45] and such an improvement comes from the low-loss nature of the Al-doped Ag films. Moreover, the propagation length can be further improved by reducing Al-doped Ag strip width and thickness, improving the cladding material properties,[46] or using multi-strip configurations.[47]

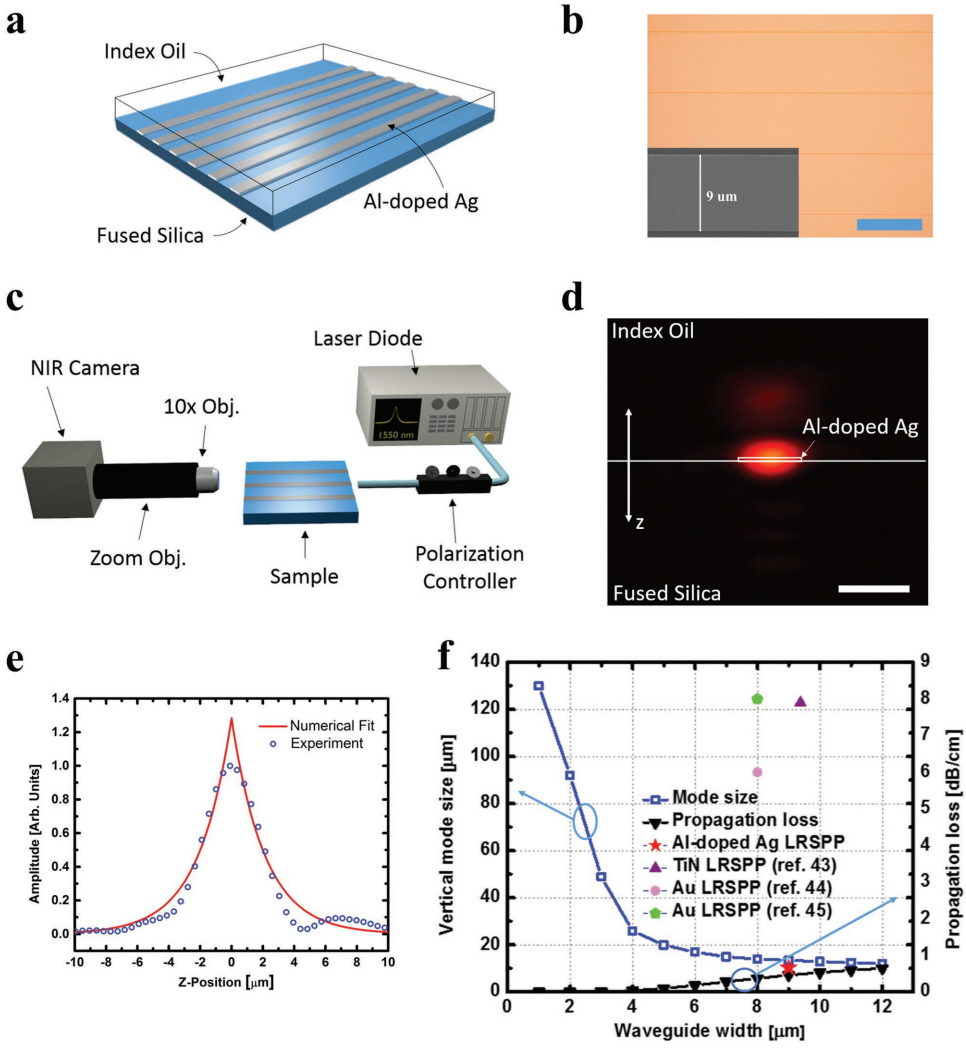

Figure 3. a) Schematic drawing of the Al-doped Ag LR-SPP waveguide. Index matching oil is used to match the refractive index of fused silica substrate at 1.55 μm. b) Optical microscope image of several fabricated Al-doped Ag LR-SPP waveguides. The insert is the SEM image of one waveguide. The scale bar is 50 μm. c) Measurement setup to characterize the mode profile and propagation loss of the waveguide. d) Experimentally measured modal profile from the output facet of the Al-doped Ag LR-SPP waveguide. The scale bar is 10 μm. e) Fitting of the vertical intensity with exponential decay of the plasmonic mode. f) Simulated mode size and propagation loss of 10 nm thick, Al-doped Ag strip waveguide with different strip widths (solid lines). The red star denotes the measured propagation loss of a 10 nm thick, 9 μm wide Al-doped Ag LR-SPP waveguide in this work. The purple triangle denotes the measured propagation loss of a 10 nm thick, 9.38 μm wide TiN LR-SPP waveguide.[43] The green pentagon and magenta circle denote the measured propagation loss from two 10 nm thick, 8 μm wide Au LR-SPP waveguides.[44,45]

The ability of forming an ultrathin layer makes Al-doped Ag an excellent material for fabricating hyperbolic metamaterials (HMMs).[48] HMMs are highly anisotropic structures which exhibit a metallic response (i.e., $\mathrm{Re}\{\varepsilon\} < 0$) in one (two) directions and a dielectric response (i.e., $\mathrm{Re}\{\varepsilon\} > 0$) in the other two (one) directions. Such a high anisotropy endows HMMs with a theoretically unbounded hyperbolic dispersion and thus, an ultrahigh photonic density of states (PDOS). Because of their peculiarities, HMMs have been used to demonstrate broadband absorption,[49] enhanced spontaneous emission,[50] and engineered thermal radiation.[51]

One way to fabricate HMMs is by depositing alternating layers of metal and dielectric thin films, leading to a dielectric response (i.e., $\mathrm{Re}\{\varepsilon_\perp\} > 0$) in the direction normal to the layers and a metallic response (i.e., $\mathrm{Re}\{\varepsilon_\parallel\} < 0$) in-plane. The electromagnetic response of such HMMs is described by an effective magnetic permeability equal to the free-space value, and an effective electric permittivity in the tensor form: $\varepsilon_{\mathrm{eff}} = \begin{pmatrix} \varepsilon_\parallel & 0 & 0 \\ 0 & \varepsilon_\parallel & 0 \\ 0 & 0 & \varepsilon_\perp \end{pmatrix}$, where $\varepsilon_\parallel$ and $\varepsilon_\perp$ are complex values ($\varepsilon_\parallel = \varepsilon'_\parallel + i\varepsilon''_\parallel$ and $\varepsilon_\perp = \varepsilon'_\perp + i\varepsilon''_\perp$). The dispersion relation of HMMs is given by: $k_x^2/\varepsilon_\perp + k_z^2/\varepsilon_\parallel = k_0^2$, where k_x and k_z are the complex amplitudes of the transverse and normal components of the complex wave-vector, and k_0 is the free-space wave-vector (with respect to the coordinate system in **Figure 4**a). Since $\varepsilon'_\parallel < 0$ and $\varepsilon'_\perp > 0$, HMMs are governed by hyperbolic isofrequency curves and allow for the propagation of modes with transverse wave-vectors k_x larger than free-space wave-vector k_0 (high-k

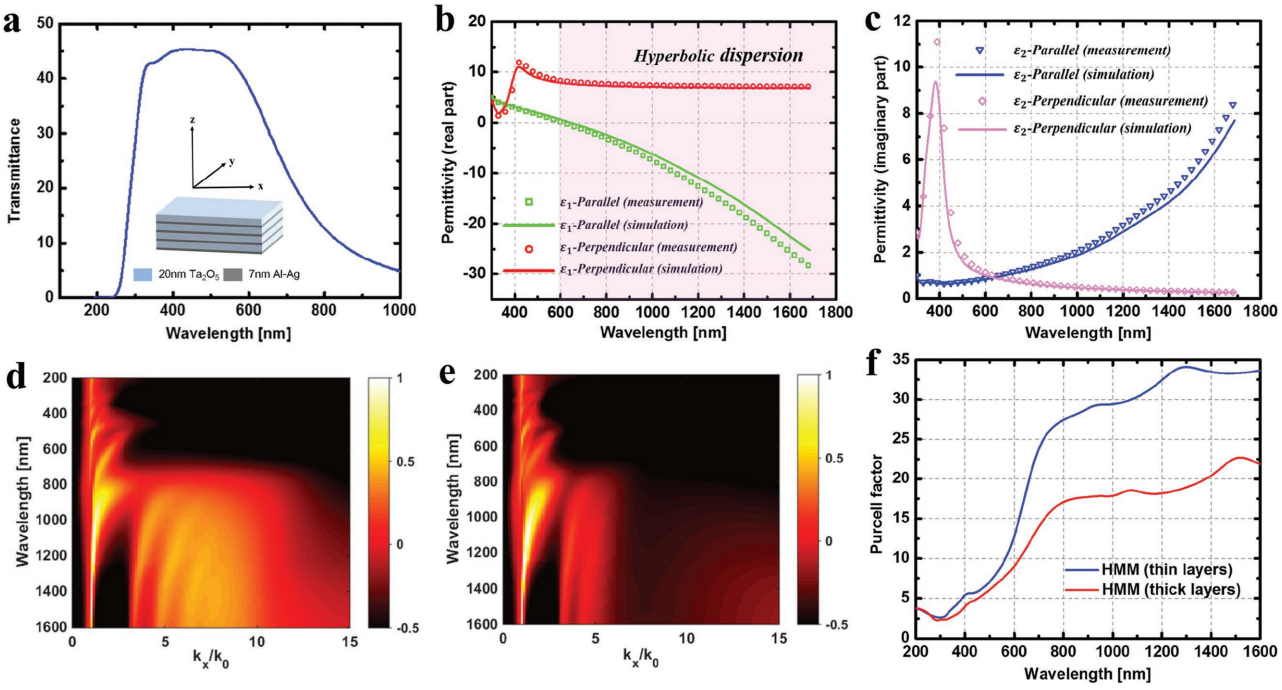

Figure 4. a) Measured transmission efficiency from the fabricated HMM consisting of 4 periods of 7 nm Al-doped Ag and 20 nm Ta_2O_5. The insert is a schematic drawing. b) Simulated (solid curve) and measured (dotted curve) real part of the permittivity of the fabricated HMM. The permittivity along the parallel direction turns negative beyond 610 nm and therefore, the HMM has a hyperbolic dispersion (denoted by the shaded area). c) Simulated (solid curve) and measured (dotted curve) imaginary part of the permittivity of the fabricated HMM. d) Calculated transmission amplitude of an electromagnetic wave with different transverse wave-vectors (k_x) through an HMM made of 8 periods of 7 nm Al-doped Ag and 20 nm Ta_2O_5. e) Calculated transmission amplitude of an electromagnetic wave with different transverse wave-vectors (k_x) through a HMM made of 4 periods of 14 nm Al-doped Ag and 40 nm Ta_2O_5. f) Calculated Purcell factor of a dipole emitter located 10 nm above the two HMMs studied in (d) and (e). The Purcell factor is averaged over different dipole orientations (two-third contribution from parallel dipoles and one-third contribution from vertical dipoles).

modes, Section S5.1, Supporting Information). However, in practice there is a limit to the maximum allowed high-k mode, and this limit is determined by the inverse of the unit cell size, i.e., $\Lambda = t_{metal} + t_{dielectric}$, where t_{metal} and $t_{dielectric}$ is the thickness of metal and dielectric layer in one unit cell, respectively. This is because at large values of k_x, the normal wave-vector k_z is also large (consistent with the hyperbolic dispersion). Consequently, the effective wavelength ($\lambda_z = 2\pi/k_z$) along the normal direction is comparable with the unit size cell and therefore, the effective medium theory approximation breaks down. Instead, the photonic band structures originating from the multilayer configurations of HMMs should be considered, which seriously compromises the ultrahigh PDOS predicted by HMM's theoretical hyperbolic dispersion. Therefore, it is desirable to have thin constituent layers in HMMs. However, since it is challenging to obtain thin and smooth Ag films, most reported HMMs use relatively thick (and rough) Ag films, and suffer from a lossy and nonhomogeneous response (e.g., transmission spectra with oscillating features which deviate from effective medium theory[52]). In contrast, our ultrathin and smooth Al-doped Ag films greatly improve upon these limitations, facilitating the fabrication of low-loss and homogeneous HMMs with a high transmittance, small unit cell size, and optical properties which are well approximated by effective medium theory.

The fabricated HMM consists of four periods (alternating layers of 7 nm Al-doped Ag and 20 nm Ta_2O_5) starting with the Al-doped Ag film on the fused silica substrate (inset of Figure 4a). The measured transmission at normal incidence is plotted in Figure 4a. It has both a high and smooth transmittance across the visible range, which benefits from the ultrathin, smooth, and low-loss metallic layer. The structure's optical properties were characterized using spectroscopic ellipsometry (M-2000, J. A. Woollam Co.), where the HMM was modeled as a uniaxial anisotropic medium with different in-plane (parallel) and out-of-plane (perpendicular) optical constants. The simulated and measured permittivities are plotted in Figure 4b,c (real and imaginary part, respectively), which show a close correspondence with each other. In the parallel direction, the epsilon near zero point is around 610 nm, and beyond this wavelength, the HMM's dispersion transitions from an ellipsoidal to a hyperbolic behavior.

As mentioned earlier, the maximal allowed high spatial wave-vectors (high-k modes) in HMMs are determined by the inverse of its unit cell size. One way to see this is by examining the transmission amplitude of an electromagnetic wave with a large value k_x through a HMM. Figure 4d,e shows the transmission amplitudes of modes with different k_x values through two HMMs, which have an identical thickness and ratio of metal–dielectric layers, but a different unit cell size. The HMM considered in Figure 4d consists of 8 periods of 7 nm Al-doped Ag and 20 nm Ta_2O_5, while the HMM in Figure 4e consists of 4 periods of 14 nm Al-doped Ag and 40 nm Ta_2O_5. Although these HMMs have identical ratios and total thicknesses of metal and dielectric layers (thus identical behaviors predicted

by the effective media theory), the HMM with thinner constituent layers supports a much broader transmission band for high-*k* modes, which contributes to its larger PDOS.[53] A high PDOS is essential to many extraordinary phenomena enabled by HMMs (e.g., broadband absorption, enhanced spontaneous/stimulated emission, engineered thermal radiation, etc.). As an example, for a dipole emitter located 10 nm above the HMM, the Purcell enhancement factor of the emitter on top of HMM with thinner layers is about two times higher than that of the emitter on top of HMM with thicker layers (Figure 4f; calculation details are given in Section S5.2 of the Supporting Information).[54]

Besides applications in HMMs, the ultrathin, smooth, low-loss, and stable Al-doped Ag will also benefit similar structures where the planar Ag films are used, such as negative refractive index metamaterials, superlenses, and transparent conductors. Transparent conductors have numerous applications in displays, solar cells, and light emitting diodes. Currently, one of the most widely used transparent conductors is indium tin oxide (ITO); however, it suffers from issues, such as poor mechanical flexibility, limited conductivity over large areas, scarcity of the indium element, and toxicity.[55,56] In light of these limitations, many ITO-free, transparent conductors have been investigated, including thin metal films,[57,58] nanostructured metallic structures,[59,60] carbon nanotubes,[61] graphene,[62] and ploy (3,4-ethylenedioxythiophene) polystyrene sulfonate (PEDOT:PSS)[63] Compared to other ITO-free electrodes, thin metal films have the advantages of simplified fabrication, low-cost, and being highly conductive and defect-free over large areas. Here, we give an example of using Al-doped Ag films to construct ITO-free transparent conductors. Our ultrathin, smooth, and low-loss Al-doped Ag film itself provides high transmission over the visible spectrum, giving an averaged transmission of 73.9% from 400 to 1000 nm for a 7 nm thick film (**Figure 5**b). The transmission gradually drops toward the longer wavelength, mainly because of the increased reflection from the metal film. Indeed, such an increased reflection can be utilized for resonant light harvesting in organic solar cells, therefore enhancing the devices' power conversion efficiencies.[25] However, in order to be employed in universal device configurations, thin films are desired to have a high transmittance.

One strategy to increase transmittance (reduce reflection) of a thin metal film is to employ a dielectric–metal–dielectric (DMD) structure, whose schematic is plotted in Figure 5a. An ultrathin Al-doped Ag film is sandwiched between two titanium dioxide (TiO_2) layers, and an additional layer of magnesium fluoride (MgF_2) is deposited on top of the upper TiO_2 layer to further suppress the reflection. With a given thickness of the Al-doped Ag layer, the thicknesses of the other three layers (e.g., TiO_2 and MgF_2) can be adjusted in order to achieve a high transmittance over a certain wavelength range. It is worth noting that such a transmission enhancement is induced by

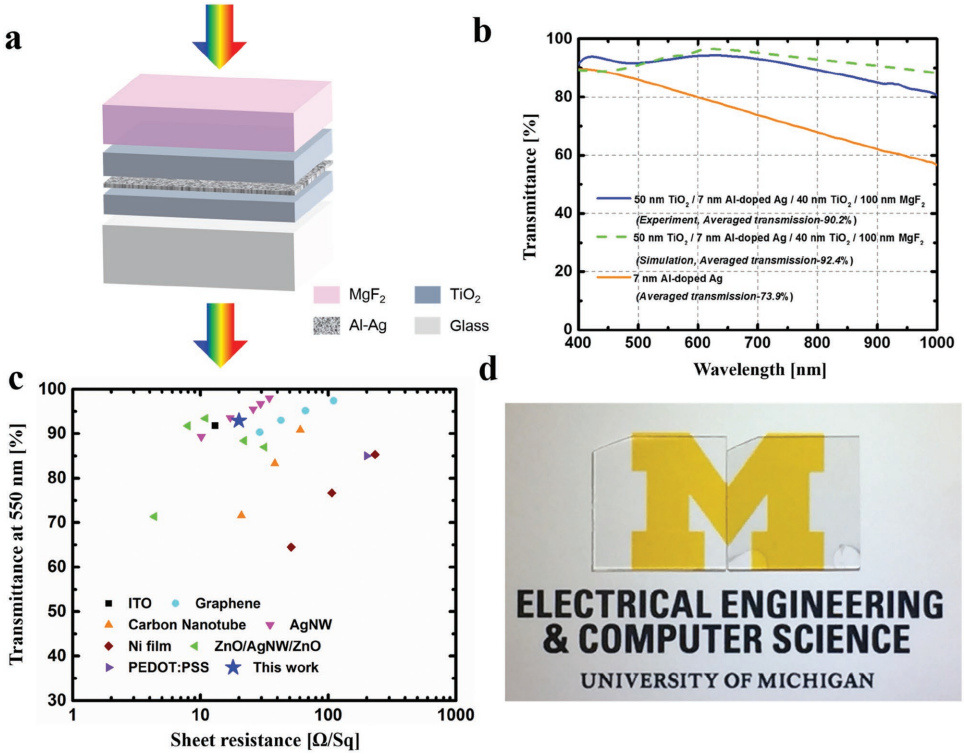

Figure 5. a) Schematic drawing of an Al-doped Ag based transparent conductor using dielectric/metal/dielectric (DMD) configuration. b) Measured (solid line) and simulated (dotted line) transmittance of the designed transparent conductor (50 nm TiO_2/7 nm Al-doped Ag/40 nm TiO_2/100 nm MgF_2). The measured transmittance through a bare 7 nm Al-doped Ag film is also plotted as a comparison. c) Comparison of optical transmittance (at 550 nm) versus sheet resistance for our work and other reported transparent conductors, such as ITO, graphene,[62] carbon nanotube,[61] silver nanowire (AgNW),[59] nickel thin film,[58] ZnO/Ag nanowire/ZnO composite electrode,[60] and PEDOT:PSS.[63] d) Left: image of a bare fused silica substrate; Right: image of an Al-doped Ag based transparent conductor (50 nm TiO_2/7 nm Al-doped Ag/40 nm TiO_2/100 nm MgF_2).

multiple optical resonances within the dielectrics, and the detailed analysis is listed in Section S6.1 of the Supporting Information. In this study, the goal is to achieve a high transmittance from the DMD structure over the visible and near-IR range (from 400 to 1000 nm). An optimized DMD stack of 45 nm TiO_2/7 nm Al-doped Ag/40 nm TiO_2/100 nm MgF_2 provides a both high and flat transmittance over this range, giving an averaged transmittance of 92.4%. The measured spectrum of the fabricated structure is plotted in Figure 5b, in a good correspondence with simulation. The images of a bare fused silica substrate (left one) and a transparent conductor based on a 7 nm Al-doped Ag film (right one) are shown in Figure 5d, both of which have similar appearances. The sheet resistance of the sample was measured as 20 Ω^{-1}. The performance of Al-doped Ag based transparent conductor is also compared to other types of transparent conductors (e.g., ITO, graphene, carbon nanotube, metal mesh, thin metal film, PEDOT:PSS, etc.) in terms of their conductivity and transmittance (at 550 nm), where Al-doped Ag based transparent conductor shows a superior or comparable performance (Figure 5c). Besides the high optical transparency and good electrical conductivity, Al-doped Ag also has the advantage of smooth surface morphology compared to pure Ag, which contributes to the reliability of optoelectronic devices. Since the thickness of many optoelectronic devices (especially organic optoelectronic devices) is only on the order of a few hundred nanometers, a rough surface could easily result in electrical shorts between electrodes, especially for large-area devices.[64] Devices with rough electrodes are prone to exhibit low efficiencies due to the current shunt paths which produce a higher dark current.[65] The smooth Al-doped Ag film is of significance in providing a simple solution to overcome this problem. At last, it is worth noting that such a DMD design also applies to thicker Ag films; however, due to the increased absorption associated with thicker metal films, the optimized transmission is reduced (Section S6.2, Supporting Information). For example, for a 10 nm Al-doped Ag, the optimized structure of 40 nm TiO_2/10 nm Al-doped Ag/35 nm TiO_2/70 nm MgF_2 gives out an averaged transmittance of 87.4% from 400 to 1000 nm. The transmission is even lower for structures with 13 and 16 nm Al-doped Ag films (averaged transmittance of 80.1% and 71.7%, respectively).

In this work, various high-performance nanophotonic devices based on Al-doped Ag have been demonstrated. Thin Al-doped Ag film maintains the excellent optical properties of pure Ag, and at the same time, significantly outperforms thin pure Ag film in terms of surface smoothness, long-term and thermal stability, as well as adhesion with the substrate. For all these reasons, Al-doped Ag can be the key for the realization of several nanophotonic devices that could not be attained by using standard Ag. First, we show that LR-SPP waveguides made of Al-doped Ag exhibit a propagation distance of few centimeters, which is almost one order of magnitude better compared to the propagation distance of LR-SPP waveguides made of other plasmonic materials. Second, hyperbolic metamaterials consisting of ultrathin Al-doped Ag films can be attained having a homogeneous and low-loss response, and supporting a broad range of high-k modes as a direct consequence of the nanometric thickness and superior uniformity of the constituent layers. Finally, transparent conductors based on Al-doped Ag are demonstrated and proved to possess both a high and flat transmittance over the visible and near-IR range.

In addition to the aforementioned devices, many other nanophotonic structures can certainly benefit from our Al-doped Ag. For example, there has been a recent interest in designing nanostructures with complex geometries for versatile light property control.[6,66,67] However, the rough morphology and poor stability of pure Ag films prohibit practical manufacturing of these designs. Al-doped Ag provides a viable solution for fabrication of such devices, due to its smooth surface morphology and great stability. Similarly, Al-doped Ag may also facilitate the fabrication of 3D metamaterials (fishnet structures,[68] Ag-coated plasmonic nanoantennas[69]), as well as plasmon-induced hot electron devices.[70] In conclusion, owing to its unprecedented quality, stability, smoothness, and simple room-temperature deposition method, Al-doped Ag overcomes the fundamental material limits of pure Ag, and may hold the potential to form the foundation of a high-performance nanophotonic framework.

Experimental Section

Al-Doped Ag Film Growth: The Al-doped Ag films were cosputtered on fused silica substrates by a DC magnetron sputter tool (Lab18, Kurt J. Lesker Co.) with Argon (Ar) gas at room temperatures. The chamber base pressure was pumped down to about 1×10^{-6} Torr before the film deposition. During deposition, the Ar gas pressure was 4.5 mTorr and the substrate holder was rotated at a rate of 10 rpm. Two pure Ag and Al targets were cosputtered to create Al-doped Ag films. By varying the source powers for Al and Ag targets, the composition of sputtered films was adjusted. The sputtering rates of Ag at 1.109 nm s^{-1} and Al at 0.072 nm s^{-1} produce Al-doped Ag films with optimized optical properties.

Device Fabrication: To fabricate the LR-SPP waveguide, a 10 nm thick, Al-doped Ag film was first deposited on a fused silica substrate by Al and Ag codeposition. Subsequently, to further reduce its loss, the film underwent an annealing treatment (500 °C for 10 s in N_2 environment). Photolithography (GCA AS200 AutoStep) was used to define the waveguide shape in the photoresist (SPR 220.3, MicroChem). Afterward, the pattern was transferred into the Al-doped Ag film by an argon (Ar) ion-bombardment etching (STS Pegasus ICP). Finally, the photoresist was removed by acetone with the aid of ultrasound sonication. As mentioned in the main context, Al-doped Ag films have good adhesion with substrates and are robust against commonly used chemicals during the nanofabrication. These properties contribute to the fabrication of Al-doped Ag based LR-SPP waveguides. The fabricated Al-doped Ag LRSP waveguide had a width of 9 μm and thickness of 10 nm.

Sample and Device Characterization: The optical properties of Al-doped Ag were characterized by spectroscopic ellipsometry using the reflection plus transmission method.[71] The optical properties of the HMM were characterized using the spectroscopic ellipsometer (M-2000, J. A. Woollam Co.), where the HMM was modeled as a uniaxial anisotropic medium with different in-plane (parallel) and out-of-plane (perpendicular) optical constants. The transmission spectra of both HMM and transparent conductor were characterized by the spectroscopic ellipsometer in its transmission mode.

The STEM was characterized on JEOL 3100R05 Cs-corrected analytical electron microscope and JEOL JEM-2800 high throughput TEM/STEM/SEM. To prepare the sample for STEM, the surface of the film was first covered by a piece of polished Si substrate with M-bond 610 adhesive. The adhesive was cured by baking on a hotplate at 120 °C for 3 h. This fused silica/Al-doped Ag/Si clad was then cut into slices of cross-sectional specimen. The specimen was then grinded on the diamond lapping paper followed by ion milling. The final specimen was about 50 nm in thickness for the STEM characterization.

The LR-SPP waveguide performance was characterized by the fiber end-coupling method (Figure 3c) when cladded by an index matching oil (Code 50350, Cargille Labs). A 1.55 µm laser light (8164A, Agilent technologies) was coupled into a polarization controller (FPC032, Thorlabs) and guided in a polarization maintaining fiber (P3-1550PM-FC-5, Thorlabs) as a TM mode (polarization in the vertical direction). The output from the LR-SPP waveguide was collected by an objective (Corrected 10×, Mitutoyo Infinity) and observed by an infrared camera (XEVA-1.7-320, Xenics), which was also calibrated to serve as a power meter. To measure the propagation loss of the waveguide, output power from waveguides of different lengths were recorded (cut-back method).

Supporting Information

Supporting Information is available from the Wiley Online Library or from the author.

Acknowledgements

This work was supported by the NSF Materials Research Science and Engineering Center (MRSEC) Program DMR 1120923, NSF grant DMR 1506535, and AFOSR grant FA9550-14-1-0138. The study of transparent conducting electrode was supported by the Beijing Institute of Collaborative Innovation (BICI). C. Zhang, L. Chen, C. Ji, and L. J. Guo acknowledge the technical support from the Lurie Nanofabrication Facility (LNF) at the University of Michigan. The STEM work was performanced at the Irvine Materials Research Insititue (IMRI) at University of California-Irvine. C. Zhang acknowledges the discussion with Dr. Nina Hong, Dr. Deen Gu, Dr. You-Chia Zhang, and Mr. Mingfei Zhang.

Received: September 25, 2016
Revised: January 31, 2017
Published online:

[1] V. Giannini, A. I. Fernández-Domínguez, S. C. Heck, S. A. Maier, *Chem. Rev.* **2011**, *111*, 3888.
[2] J. A. Schuller, E. S. Barnard, W. Cai, Y. C. Jun, J. S. White, M. L. Brongersma, *Nat. Mater.* **2010**, *9*, 193.
[3] Y. Liu, X. Zhang, *Chem. Soc. Rev.* **2011**, *40*, 2494.
[4] H. J. Lezec, J. A. Dionne, H. A. Atwater, *Science* **2007**, *316*, 430.
[5] N. Fang, H. Lee, C. Sun, X. Zhang, *Science* **2005**, *308*, 534.
[6] N. Yu, F. Capasso, *Nat. Mater.* **2014**, *13*, 139.
[7] Y.-K. R. Wu, A. E. Hollowell, C. Zhang, L. J. Guo, *Sci. Rep.* **2013**, *3*, 1194.
[8] J. B. Pendry, D. Schurig, D. R. Smith, *Science* **2006**, *312*, 1780.
[9] S. Law, C. Roberts, T. Kilpatrick, L. Yu, T. Ribaudo, E. A. Shaner, V. Podolskiy, D. Wasserman, *Phys. Rev. Lett.* **2014**, *112*, 017401.
[10] G. V. Naik, J. L. Schroeder, X. Ni, A. V. Kildishev, T. D. Sands, A. Boltasseva, *Opt. Mater. Express* **2012**, *2*, 478.
[11] M. A. Noginov, L. Gu, J. Livenere, G. Zhu, A. K. Pradhan, R. Mundle, M. Bahoura, Y. A. Barnakov, V. A. Podolskiy, *Appl. Phys. Lett.* **2011**, *99*, 021101.
[12] A. N. Grigorenko, M. Polini, K. S. Novoselov, *Nat. Photonics* **2012**, *6*, 749.
[13] K. M. McPeak, S. V. Jayanti, S. J. P. Kress, S. Meyer, S. Iotti, A. Rossinelli, D. J. Norris, *ACS Photonics* **2015**, *2*, 326.
[14] Y. Wu, C. Zhang, N. M. Estakhri, Y. Zhao, J. Kim, M. Zhang, X.-X. Liu, G. K. Pribil, A. Alù, C.-K. Shih, X. Li, *Adv. Mater.* **2014**, *26*, 6106.
[15] A. Goswami, *Thin Film Fundamentals*, New Age International Publishers, New Delhi, India **1996**.
[16] S. Laref, J. Cao, A. Asaduzzaman, K. Runge, P. Deymier, R. W. Ziolkowski, M. Miyawaki, K. Muralidharan, *Opt. Express* **2013**, *21*, 11827.
[17] J. Gong, R. Dai, Z. Wang, Z. Zhang, *Sci. Rep.* **2015**, *5*, 9279.
[18] M. G. Blaber, M. D. Arnold, M. J. Ford, *J. Phys.: Condens. Matter* **2010**, *22*, 143201.
[19] R. S. Sennett, G. D. Scott, *J. Opt. Soc. Am.* **1950**, *40*, 203.
[20] V. J. Logeeswaran, N. P. Kobayashi, M. S. Islam, W. Wu, P. Chaturvedi, N. X. Fang, S. Y. Wang, R. S. Williams, *Nano Lett.* **2009**, *9*, 178.
[21] H. Im, S. H. Lee, N. J. Wittenberg, T. W. Johnson, N. C. Lindquist, P. Nagpal, D. J. Norris, S.-H. Oh, *ACS Nano* **2011**, *5*, 6244.
[22] K. Thürmer, E. D. Williams, J. E. Reutt-Robey, *Phys. Rev. B* **2003**, *68*, 155423.
[23] H. C. Kim, T. L. Alford, D. R. Allee, *Appl. Phys. Lett.* **2002**, *81*, 4287.
[24] D. Gu, C. Zhang, Y.-K. Wu, L. J. Guo, *ACS Nano* **2014**, *8*, 10343.
[25] C. Zhang, D. Zhao, D. Gu, H. Kim, T. Ling, Y.-K. R. Wu, L. J. Guo, *Adv. Mater.* **2014**, *26*, 5696.
[26] P. Berini, *Adv. Opt. Photonics* **2009**, *1*, 484.
[27] T. Nikolajsen, K. Leosson, S. I. Bozhevolnyi, *Appl. Phys. Lett.* **2004**, *85*, 5833.
[28] A. Boltasseva, S. I. Bozhevolnyi, *IEEE J. Quantum Electron.* **2006**, *12*, 1233.
[29] O. Krupin, H. Asiri, C. Wang, R. N. Tait, P. Berini, *Opt. Express* **2013**, *21*, 698.
[30] S. Butun, K. Aydin, *ACS Photonics* **2015**, *2*, 1652.
[31] H. Liu, B. Wang, E. S. P. Leong, P. Yang, Y. Zong, G. Si, J. Teng, S. A. Maier, *ACS Nano* **2010**, *4*, 3139.
[32] N. P. Sergeant, A. Hadipour, B. Niesen, D. Cheyns, P. Heremans, P. Peumans, B. P. Rand, *Adv. Mater.* **2012**, *24*, 728.
[33] P. Wróbel, T. Stefaniuk, M. Trzcinski, A. A. Wronkowska, A. Wronkowski, T. Szoplik, *ACS Appl. Mater. Interfaces* **2015**, *7*, 8999.
[34] X. Jiao, J. Goeckeritz, S. Blair, M. Oldham, *Plasmonics* **2009**, *4*, 37.
[35] T. G. Habteyes, S. Dhuey, E. Wood, D. Gargas, S. Cabrini, P. J. Schuck, A. P. Alivisatos, S. R. Leone, *ACS Nano* **2012**, *6*, 5702.
[36] A. Kossoy, V. Merk, D. Simakov, K. Leosson, S. Kéna-Cohen, S. A. Maier, *Adv. Opt. Mater.* **2015**, *3*, 71.
[37] S. Auer, W. Wan, X. Huang, A. G. Ramirez, H. Cao, *Appl. Phys. Lett.* **2011**, *99*, 041116.
[38] S. A. Maier, *Plasmonics: Fundamentals and Applications*, Springer, New York, USA **2007**.
[39] D. A. Bobb, G. Zhu, M. Mayy, A. V. Gavrilenko, P. Mead, V. I. Gavrilenko, M. A. Noginov, *Appl. Phys. Lett.* **2009**, *95*, 151102.
[40] C. Gong, M. S. Leite, *ACS Photonics* **2016**, *3*, 507.
[41] C. Gong, M. R. S. Dias, G. C. Wessler, J. A. Taillon, L. G. Salamanca-Riba, M. S. Leite, *Adv. Opt. Mater.* **2017**, *5*, 1600568.
[42] Phase Diagram Software from the National Physical Laboratory, UK, http://resource.npl.co.uk/mtdata/phdiagrams/agal.htm (accessed: January 2017).
[43] N. Kinsey, M. Ferrera, G. V. Naik, V. E. Babicheva, V. M. Shalaev, A. Boltasseva, *Opt. Express* **2014**, *22*, 12238.
[44] A. Boltasseva, T. Nikolajsen, K. Leosson, K. Kjaer, M. S. Larsen, S. I. Bozhevolnyi, *J. Lightwave Technol.* **2005**, *23*, 413.
[45] T. Nikolajsen, K. Leosson, I. Salakhutdinov, S. I. Bozhevolnyi, *Appl. Phys. Lett.* **2003**, *82*, 668.
[46] J. Jiang, C. L. Callender, S. Jacob, J. P. Noad, S. Chen, J. Ballato, J. D. W. Smith, *Appl. Opt.* **2008**, *47*, 3892.
[47] P. Berini, R. Charbonneau, N. Lahoud, G. Mattiussi, *J. Appl. Phys.* **2005**, *98*, 043109.
[48] A. Poddubny, I. Iorsh, P. Belov, Y. Kivshar, *Nat. Photonics* **2013**, *7*, 948.

[49] D. Ji, H. Song, X. Zeng, H. Hu, K. Liu, N. Zhang, Q. Gan, *Sci. Rep.* **2014**, *4*, 4498.
[50] D. Lu, J. J. Kan, E. E. Fullerton, Z. Liu, *Nat. Nanotechnol.* **2014**, *9*, 48.
[51] P. N. Dyachenko, S. Molesky, A. Y. Petrov, M. Störmer, T. Krekeler, S. Lang, M. Ritter, Z. Jacob, M. Eich, *Nat. Commun.* **2016**, *7*, 11809.
[52] G. Subramania, A. J. Fischer, T. S. Luk, *Appl. Phys. Lett.* **2012**, *101*, 241107.
[53] L. Gu, T. U. Tumkur, G. Zhu, M. A. Noginov, *Sci. Rep.* **2014**, *4*, 4969.
[54] G. W. Ford, W. H. Weber, *Phys. Rep.* **1984**, *113*, 195.
[55] O. Inganas, *Nat. Photonics* **2011**, *5*, 201.
[56] D. Lison, J. Laloy, I. Corazzari, J. Muller, V. Rabolli, N. Panin, F. Huaux, I. Fenoglio, B. Fubini, *Toxicol. Sci.* **2009**, *108*, 472.
[57] G. Zhao, W. Wang, T.-S. Bae, S.-G. Lee, C. Mun, S. Lee, H. Yu, G.-H. Lee, M. Song, J. Yun, *Nat. Commun.* **2015**, *6*, 8830.
[58] D. S. Ghosh, L. Martinez, S. Giurgola, P. Vergani, V. Pruneri, *Opt. Lett.* **2009**, *34*, 325.
[59] D.-S. Leem, A. Edwards, M. Faist, J. Nelson, D. D. C. Bradley, J. C. de Mello, *Adv. Mater.* **2011**, *23*, 4371.
[60] A. Kim, Y. Won, K. Woo, C.-H. Kim, J. Moon, *ACS Nano* **2013**, *7*, 1081.
[61] D. S. Hecht, L. Hu, G. Irvin, *Adv. Mater.* **2011**, *23*, 1482.
[62] S. Bae, H. Kim, Y. Lee, X. Xu, J.-S. Park, Y. Zheng, J. Balakrishnan, T. Lei, H. Ri Kim, Y. I. Song, Y.-J. Kim, K. S. Kim, B. Ozyilmaz, J.-H. Ahn, B. H. Hong, S. Iijima, *Nat. Nanotechnol.* **2010**, *5*, 574.
[63] D. Gupta, M. M. Wienk, R. A. J. Janssen, *Adv. Energy Mater.* **2013**, *3*, 782.
[64] N. Wang, J. D. Zimmerman, X. Tong, X. Xiao, J. Yu, S. R. Forrest, *Appl. Phys. Lett.* **2012**, *101*, 133901.
[65] J.-Y. Lee, S. T. Connor, Y. Cui, P. Peumans, *Nano Lett.* **2008**, *8*, 689.
[66] C. Zhang, C. Pfeiffer, T. Jang, V. Ray, M. Junda, P. Uprety, N. Podraza, A. Grbic, L. J. Guo, *Laser Photonics Rev.* **2016**, *10*, 791.
[67] A. V. Kildishev, A. Boltasseva, V. M. Shalaev, *Science* **2013**, *339*, 339.
[68] D. Chanda, K. Shigeta, S. Gupta, T. Cain, A. Carlson, A. Mihi, A. J. Baca, G. R. Bogart, P. Braun, J. A. Rogers, *Nat. Nanotechnol.* **2011**, *6*, 402.
[69] C. E. Hofmann, F. J. García de Abajo, H. A. Atwater, *Nano Lett.* **2011**, *11*, 372.
[70] M. L. Brongersma, N. J. Halas, P. Nordlander, *Nat. Nanotechnol.* **2015**, *10*, 25.
[71] J. N. Hilfiker, N. Singh, T. Tiwald, D. Convey, S. M. Smith, J. H. Baker, H. G. Tompkins, *Thin Solid Films* **2008**, *516*, 7979.